IEEE Access
Multidisciplinary : Rapid Review : Open Access Journal

Received October 4, 2018, accepted October 12, 2018, date of publication October 22, 2018, date of current version November 19, 2018.

Digital Object Identifier 10.1109/ACCESS.2018.2877157

Developing a PSO-Based Projection Algorithm for a Porosity Detection System Using X-Ray CT Images of Permeable Concrete

YI-ZENG HSIEH[1], MU-CHUN SU[2], JIEH-HAUR CHEN[3], BEVAN ANNUERINE BADJIE[3], AND YU-MIN SU[4]

[1]Department of Electrical Engineering, National Taiwan Ocean University, Keelung 20224, Taiwan
[2]Department of Computer Science and Information Engineering, National Central University, Taoyuan 32001, Taiwan
[3]Institute of Construction Engineering and Management, National Central University, Taoyuan 32001, Taiwan
[4]Department of Civil Engineering, National Kaohsiung University of Applied Sciences, Kaohsiung 80778, Taiwan

Corresponding author: Jieh-Haur Chen (jhchen@ncu.edu.tw)

This work was supported by the Ministry of Science and Technology, Taiwan, for promoting academic excellent of universities under Grant MOST-105-2221-E-008-113, Grant 106-2221-E-008-020-MY2, Grant 107-2221-E-008-084-MY2, Grant 107-2634-F-008-001, Grant 106-2634-F-038-002, Grant 107-2221-E-019-039-MY2, and Grant 107-2634-F-019-001.

ABSTRACT Permeable concrete is widely used as a road surfacing material due to its sturdiness and ability to be quickly repaired. The porosity of concrete has been used as a predictive indicator for the properties of the concrete. Traditional methods for measuring this porosity are feasible but can be time-consuming. In this paper, we propose a particle swarm optimization-based projection algorithm for visualization of the high-dimensional data as a 2-D scatter plot for detecting porosity in permeable concrete from X-ray computerized tomography images. We regard the proposed projection algorithm as an improved version of Sammon's nonlinear mapping. The projected scatter plot allows for a straightforward analysis of the inherent structure of clusters within scanned images. Several data sets, including artificial data sets and real-life imaging data, were tested to demonstrate the performance of the proposed projection algorithm. The model created in this paper can augment the traditional methods for examining porosity by providing visual images for decision makers to make correct decisions for future problems. With an accuracy of $>99\%$, the visualized images provide a clearer understanding of the inner structure of pervious concrete and enhance the study of the correlation between the properties of the concrete.

INDEX TERMS Cluster analysis, projection algorithm, PSO algorithm, X-ray computerized tomography (CT), automation, computational intelligence.

I. INTRODUCTION

Porosity is an important consideration when attempting to evaluate the potential volume and permeability of asphalt concrete [1]–[4]. Asphalt concrete as used in this study is formed from thoroughly mixing heated aggregates, asphalt and dry minerals, in a specific ratio. When paving, the layers are placed on top of a finished layer then compacted to the desired compaction level [5]–[7]. Normally, when designing the concrete, experimenters need to consider the porosity, asphalt ratio, mixture strength, etc. The conventional way to quantify the porosity of the permeable concrete is to conduct manual experiment so called permeability test. By using a falling-head device, the test can determines the porosity; however, experiment repeatability is hard to reach and is also time consuming due to indistinguishable regulations in manual operation. Compared to the traditional methods used for measuring the porosity of asphalt concrete [4], [8]–[10], Computerized Tomography (CT) technology is quick, accurate and efficient [11]–[13]. Initially, CT technology's primary application was in the medical field. CT takes X-ray data scanned from the object, then uses the image reconstruction theory to calculate the structure inside the object. In 1917, Radon, an Austrian mathematician proposed the theory of how to get the cross-sectional images from image reconstruction, but it was not until 1972 that Hunsfield in England successfully used X-rays to make a computerized tomography system and proved its practicality. Each pixel of the reconstructed images corresponds to the attenuation coefficient of the scanned object. Since then, the technique has been improved by using higher energy levels and faster computation to enable the imaging of non-living specimens [11], [14], [15]. An automatic and authentic way is desired to provide practitioners with a solid porosity of tested permeable concrete cylinder(s). Therefore, this research aims to create an automatic way of detecting defects in the internal structure of a pavement material.

The objectives are to (1) develop a fully automated detection model for imaging the porosity of asphalt concrete; (2) create a method that measures the diameter of the asphalt concrete cylinder and removes the unnecessary information from the series of pictures created from CT scanning; (3) use a Particle Swarm Optimization (PSO) based projection algorithm to transform the X-ray CT images into two-dimensional scatter plots that can be used to detect the porosity in permeable concrete. By using CT-scanned images and later analyzing these images with the PSO-based projection algorithm, we achieve a more vivid representation of the positioning of the various elements in the asphalt concrete section. The positioning of the elements determines whether a pavement is bound to fail because of defects such as excessive cracks and void formation. Being able to spot potential defects within the structure of a concrete pavement allows us to come up with practical solutions as to how to effectively minimize or eliminate them.

II. POROSITY OF ASPHALT CONCRETE

After compacting, asphalt concrete consists of air, asphalt and aggregates [16]. The relationship between air, asphalt and aggregates in asphalt concrete are shown in Equation (1) where Vag = aggregate volume, Wac = asphalt weight, Wag = aggregate weight, Pac = asphalt content by percentage, Vv = void volume, Va = air volume, Vac = asphalt volume, γm = asphalt concrete specific weight, Gac = asphalt specific weight, and Gag = aggregate specific weight. The specific weight of asphalt concrete often changes with the amount of asphalt added. When there is little asphalt in the mix, the specific weight will rise. This is because of the lubrication effect which binds the aggregates and increases compaction. However, when the amount of asphalt rises to a certain level, the specific weight will start to decrease. This is because a further increase in the asphalt level will push the aggregates away, causing the specific weight to decrease [17], [18]. There are some additional important parameters for consideration of asphalt concrete weight and volume: the volume of air voids in the compacted hot mix asphalt or VTM (voids in total mix); VMA (voids in the mineral aggregate); and VFA (voids filled with asphalt). VTM is the volume of air voids after compaction of the hot mix asphalt that is the air voids between the aggregates and the asphalt. Different levels of porosity are required for different aggregate mixes and traffic loads. VMA is the sum of all the void volumes in the asphalt concrete. There are two main parts: porosity and effective asphalt content. If the VMA is too low, the concrete might have durability problems, but if the VMA is too high, there might be consistency problems. Therefore, looking at it from an economic perspective, it is not worth it [19]–[23]. The calculation for VMA is:

$$\mathrm{VMA} = 100\left(1 - \frac{\mathrm{G_{mb}}(1-\mathrm{P_b})}{\mathrm{G_{sb}}}\right), \tag{1}$$

where Gmb = asphalt bulk specific gravity; Gsb = aggregate bulk specific gravity; Pb = asphalt content.

The level of VMA affects the thickness of the film on the surface. If a suitable film thickness is not reached, the asphalt is easily oxidized and penetrated by water, which affects the tensile strength. VMA = porosity + effective asphalt content.

We calculate the VFA from the VMA and VTM. Thus,

$$\mathrm{VFA} = \frac{\mathrm{VMA} - \mathrm{VTM}}{\mathrm{VMA}} \times 100; \tag{2}$$

VTM and VMA are regulated. Although there is no specific regulation for VFA, it is actually already regulated through the VTM and VMA regulations.

III. CLUSTERING AND PSO APPLICATIONS

Clustering algorithms are effective tools for exploring the structures of complex data sets. The main goal of clustering algorithms is to dichotomize a given data set into several homogeneous clusters. Determining the optimal number of clusters has been a problem commonly encountered in engineering applications, with two approaches commonly used to solve this problem: (1) Regard the estimation of the number of clusters as a cluster validity problem, and then (2) use projection algorithms. Solving the validity problem involves increasing the number of clusters, and/or merging the existing clusters, computing certain cluster validity measures in each run, until an optimal number of clusters is obtained [24], [25]. Many different cluster validity measures have been proposed [26]–[31], such as Dunn's separation measure [26], Bezdek's partition coefficient [27], Xie-Beni's separation measure [30], Davies-Bouldin's measure [29], Gath-Geva's measure [30], etc. The projection algorithms project high-dimensional data onto a low-dimensional space to facilitate visual inspection on the data. The Sammon's algorithm is one of the popular projection algorithms [32]. Recently, several neural-network-based projection networks have also been proposed [33]–[40]. Each has its own merits and disadvantages.

PSO has been developed based on the simulation of social behavior [41]–[47]. In PSO, the performance of the individuals is continually improved by three interaction principals: cooperation, competition, and imitation among the individuals themselves through successive generations. In PSO, a particle's movement is based on the following two equations:

$$\underline{v}_i = w \times \underline{v}_i + \varphi_1 \times (\underline{p}_i - \underline{x}_i) + \varphi_2 \times (\underline{p}_g - \underline{x}_i), \tag{3}$$

$$\underline{x}_i = \underline{x}_i + \underline{v}_i, \tag{4}$$

where $\underline{v}_i$ is particle i's velocity through the parameter space, $\underline{x}_i$ is the particle's current position, $\underline{p}_i$ represents the best previous position of the ith particle, $\underline{p}_g$ is the best position found by any individual of particle i's neighborhood, w is the inertia weight. The parameters, φ_1 and φ_2, are the learning rates governing the cognition and social components, respectively. Similar to many other optimization algorithms (e.g., the genetic algorithm), the PSO must pre-specify its parameters such as the population size (i.e., the number of particles), the maximum velocity, the parameters,φ_1 and φ_2, and the topology of the swarm network (e.g., ring or star topology). Liu and Sancaktar [48] suggested that the inertial weight decreases over time, typically from approximately 0.9 to 0.4. The performance of the PSO algorithm is greatly affected by the population size and the topology of the swarm.

IV. INSTRUMENTS AND DATA COLLECTION

Computerized tomography produces a 3D image reconstructed after digital image processing. The technology involves scanning objects using X-rays. Different substances have a different radio density for X-rays. After getting the corresponding gray scale value, we can obtain a projection of the cross-sectional images of the scanned objects. By stacking the cross-sectional images using computer software, 3D images of the scanned subjects can be reconstructed. First of all, the scanning device scans the subject with X-rays to project cross-sections at different angles. Then, by application of a reconstruction algorithm, the images are reconstructed to produce 3D images of the subjects. Figure 1 illustrates the procedure for turning computerized tomography scanning into images [49].

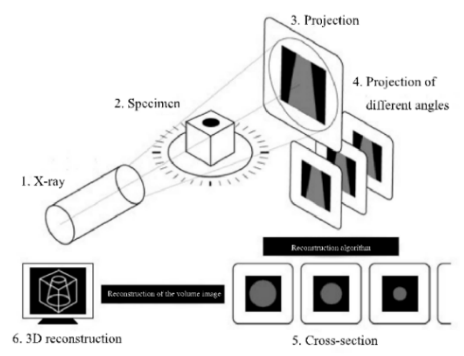

FIGURE 1. Procedure for turning CT scanning into images.

The Somatom® Emotion manufactured by Siemens Healthcare is a 16-channel X-ray CT facility that provides a maximum of 0.75 mm resolution on the Z-axis. It has the features of: Ultra-Fast Ceramic (UFC) detector, DURA 422 MV High performance CT X-ray tube, 6/16 slices, 11.7 m2 minimum installation space, and heat dissipation $<$ 7.9 kW. The specimen analysis included nondestructive evaluation with a medical X-ray CT device. We sent the specimen (concrete cylinders) to the I-shou Hospital (No.1, Yida Rd., Yanchao Dist., Kaohsiung City 824, Taiwan) for evaluation. They were placed on the patient bed during the scanning process as shown in Figure 2.

FIGURE 2. X-ray CT facility.

Prior to commencement of the scanning process, it was important that the bed be well positioned for accuracy and to facilitate the process. The process was a multiple 'in and out' process which generated multiple X-ray digital images which were then used to reconstruct the 3D images of the concrete cylinders. For the settings of the X-ray CT device, we used an 110kV with automatic current (mA/μA) to scan the concrete cylinders. We had used the same voltage and automatic current for nondestructive evaluation (NDE) scanning of plain cement concrete (PCC) or asphalt concrete in their previous works without any problems [49].

The concrete mix ratio was made up of ASTM (ASTM C150-16e1) Type I cement, clean tap water and course (siliceous) aggregates. The course aggregates had a Nominal Maximum Aggregate Size (NMAS) of 12.55, 1.35% of absorption (ASTM C127-15) with 2.64 bulk specific gravity (ASTM C127-15)). The specimens P1, P2 and P3 all had a mixing proportion of W/C at 0.30, coarse aggregates at 1530 kg/cm3, cement at 340 kg/cm3, water at 100 kg/cm3, and superplasticizer at 2 kg/cm3. P1 included a fractionated coarse aggregate retained on a 4.75mm (#4) sieve which passed through a 9.5mm (3/8 inch) sieve. P2 had a fractionated coarse aggregate retained on a 9.5mm sieve and passing through a 12.5mm (1/2 inch) sieve. P3 had a coarse aggregate comprised of a combination of the types mentioned above with no fractionation process. The three pervious concrete specimens were carefully weighted with a designated a water-cement ratio (w/c) of 0.3. The concrete cylinders were cured in lime water and the process took 28 days. To increase the workability of the concrete, super plasticizer was added during the mixing process [49]. A total 326 of CT images from dozens of concrete cylinders conveniently sampled from a pavement construction site were used for system development. Figure 3 shows CT scans of the concrete cylinders, and Figure 4 shows one of the original images.

V. AUTOMATIC DETECTION SYSTEM

The main goal of the image-processing algorithm is to locate the concrete pillar on a CT image and then compute the corresponding aperture rate. There are two major classes of optimization algorithms: (1) the derivative-based optimization

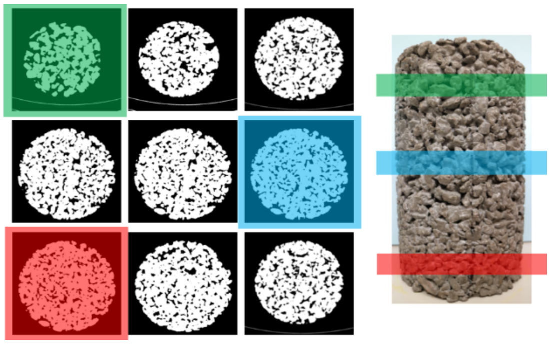

FIGURE 3. Sections through concrete cylinders scanned by medical X-ray CT and the corresponding void ratio.

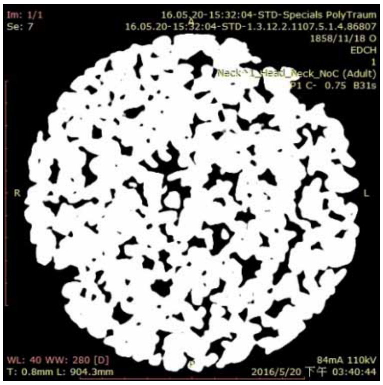

FIGURE 4. An original CT image.

algorithm which is capable of determining search directions according to an objective function's derivative information and (2) the derivative-free optimization algorithm which does not need the functional derivative information. A major concern associated with the derivative-based optimization algorithms is that they are usually apt to be trapped in the local minimum. It has motivated us to adopt the derivative-free optimization algorithm(s) to minimize the topological distance difference (TDD) function. Compared to some well-known derivative-free optimization algorithms (e.g., genetic algorithm, simulated annealing algorithm), the PSO is rather easy to be implemented and computationally efficient. Finally, we decided to adopt the PSO to minimize the TDD function. The proposed algorithm involves the following 3 steps. Step 1 Segmentation: A CT image is not a binary image as shown in Figure 4.

We may find that the image consists of a concrete pillar centered in the image and many annotated texts. In this step, we selected an appropriate threshold to transform a gray-level CT image into a binary image consisting of an object region and a background region. Correct threshold selection plays an important role in locating the object region which corresponds to the concrete pillar. The selection of the threshold is based on histogram shape analysis. The histogram of an image provides the frequency of each brightness value in the image. The histogram of the CT image shown in Figure 4 is

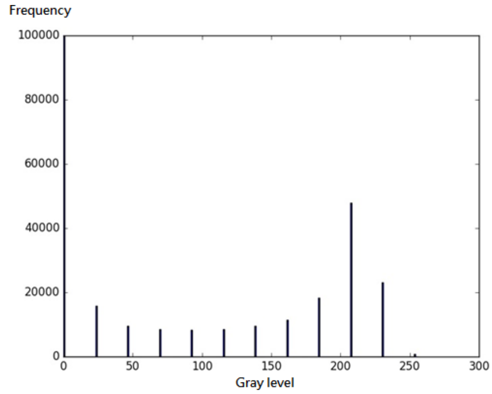

FIGURE 5. Histogram.

displayed in Figure 5. It is obvious that the histogram is bi-modal. While the object region corresponds to the right peak located at around gray value 210, the background region corresponds to the left peak located at gray value 0. Therefore, the threshold is chosen to be 200.

Based on this chosen threshold, the binary image of the CT image is then displayed in Figure 6. This threshold gives a good result for the detection of the concrete pillar from the image.

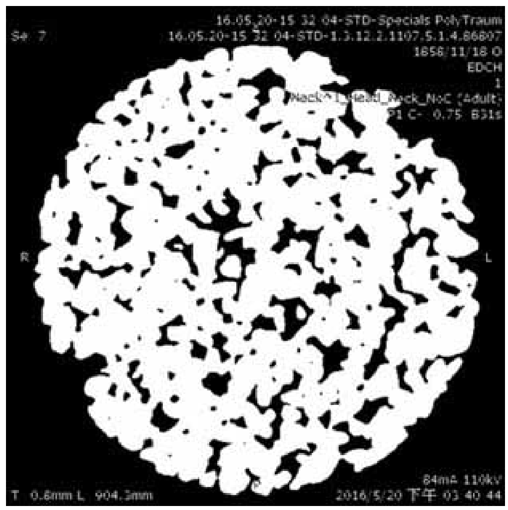

FIGURE 6. The resultant binary image.

Step 2 Deleting texts: in this step, we further segmented the concrete pillar from the binary image. We adopted the 8-connectivity property to locate the connected components in the binary image shown in Figure 7. The method for labeling connected components can be found in [39]. Without any doubt, the largest connected component corresponds to the concrete pillar; therefore, we kept the largest connected component and deleted all other connected components (e.g., the annotated texts). The segmented concrete pillar is shown in Figure 7.

Step 3 Initialization of a circle: we then chose the right circle to include the segmented concrete pillar. An easy way to

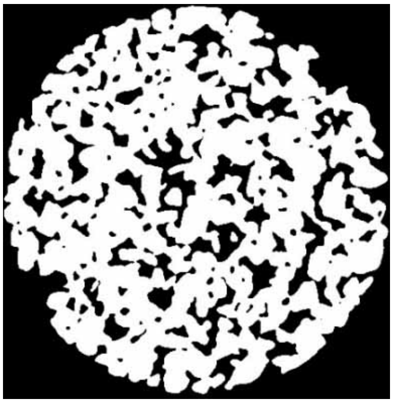

FIGURE 7. The segmented concrete pillar.

find such a circle is to find the minimum bounding rectangle for the segmented concrete pillar (as shown in Figure 8).

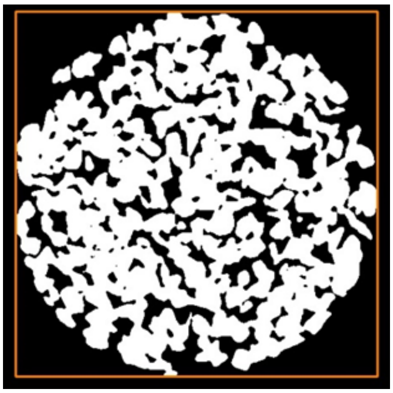

FIGURE 8. The bounding rectangle.

The center of the bounding rectangle is then used as the initial center of the circle. The average of the length and the width of the rectangle is used as the initial diameter of the circle. The resultant circle is shown in Figure 9. This initialization method is very straightforward and effective; however, it is sensitive to some disturbance factors. The

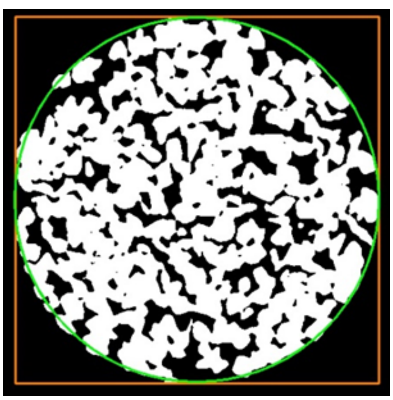

FIGURE 9. Circle computed from bounding rectangle.

disturbance factors may be attributed to the value of the threshold and the locations of the annotated texts.

For example, if the value of the threshold is specified to be too large then some data points originally belonging to the concrete pillar may be claimed to be background. In addition, if some annotated texts are connected to the pillar then these texts may be classified to be part of the pillar. An example of such a disturbed circle is shown in Fig. 10.

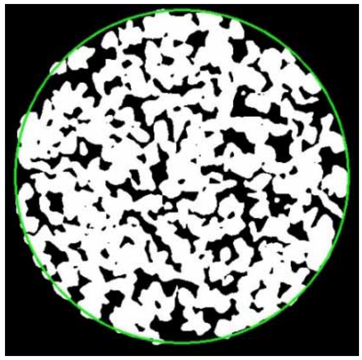

FIGURE 10. Inappropriate circle highlighted in green.

Viewing this figure, we find that there are some white points located outside the circle. Therefore, in the next step, the circle needs to be fine-tuned. Figure 8 shows the bounding rectangle around the concrete pillar used to form a circle in turn used to separate the voids and air around the cylinder. Figure 9 shows the circle formed within the bounded rectangle. The diameter of the circle is the average of the length and width of the bounded rectangle. Figure 10 shows the circle formed within the bounded rectangle, but the circle needs to be optimized for further analysis.

VI. PROPOSED PSOP ALGORITHM

The proposed PSO-based Projection (PSOP) algorithm can be regarded as an improved version of the Sammon's algorithm which is a non-linear mapping or projection algorithm. The objective of the Sammon's algorithm is to find a two-dimensional configuration of patterns in which inter-pattern distances are preserved by minimizing the following "stress" criterion:

$$E = \frac{1}{\sum_i \sum_{j>i} d(i,j)} \sum_i \sum_{j>i} \frac{[d\,(i,j) - D(i,j)]^2}{d(i,j)}, \quad (5)$$

where $d(i,j)$ denotes the distance between patterns $\boldsymbol{x}_i$ and $\boldsymbol{x}_j$ in the R^n space, $D(i,j)$ denotes the corresponding distance between patterns $\boldsymbol{p}_i$ and $\boldsymbol{p}_j$ which respectively correspond to $\boldsymbol{x}_i$ and $\boldsymbol{x}_j$ in the R^2 space. Given a data set $X = \{\boldsymbol{x}_i | \boldsymbol{x}_i \in R^n \; for \; i = 1, \ldots, N\}$, Sammon's algorithm starts with a random configuration of N patterns in R^2 space and then iteratively reconfigures the patterns via the use of the gradient-decent method to minimize the stress criterion E. Although Sammon's algorithm is straightforward, it suffers from some disadvantages (e.g., a high computational load). Several different approaches to modifying the Sammon's algorithm have been discussed [5]. For example, in order to save a significant amount of computation, Pykett proposed that only a pre-specified number of "archetypes" or centers of clusters of patterns be projected to the R^2 space. In addition, a circle is drawn around each projected archetype to facilitate the visual effect and indicate the spread of the cluster. The radius of each circle is proportional to the standard deviation of the distances between the patterns and the corresponding center of the cluster in the R^n space. The PSOP algorithm involves the following three steps:

Step 1: Adopt the k-means algorithm to cluster a given data set $X = \{x_i | x_i \in R^n \text{ for } i = 1, \ldots, N\}$ into k clusters, $c_1, \ldots, c_k$.

Step 2: Adopt the PSO algorithm to find k 2-dimentional data points, $p_1, \ldots, p_k$, such that the following topological distance difference (TDD) function is minimized:

$$\mathrm{TDD} = \sum_{i=1}^{k} \sum_{j \neq i}^{k} \left(\frac{N_i + N_j}{N} \frac{\|c_i - c_j\|}{D_{max}} - \frac{N_i + N_j}{N} \frac{\|p_i - p_j\|}{d_{max}} \right)^2, \tag{6}$$

where p_i represents the projected pattern corresponding to x_i, N_i represents the number of data points belonging to the ith cluster c_i, D_{max} represents the largest distance between two clusters in the R^n space, and d_{max} represents the largest distance between two data points in the set $p_1, \ldots, p_k$ in the R^2 space. Since we usually choose to project the N data points inside the square region, $[0, 1] \times [0, 1]$, we can set $d_{max} = \sqrt{2}$ to avoid extra computation in each iteration.

Step 3: Plot the k data points, $p_1, \ldots, p_k$, in the 2-dimentional space. Each data point is assigned a circle with the following radius r_i:

$$r_i = \frac{d_{max}}{D_{max}} R_i, \tag{7}$$

$$R_i = \frac{1}{N_i} \sum_{j=1}^{N_i} \left\| x_j^i - c_i \right\|, \tag{8}$$

where x_j^i represents the jth data point belonging to the ith cluster c_i. To some extent, R_i represents the spread of ith cluster c_i in the R^n space. Through (4), we can establish a reasonable scaling relationship between the spread of the clusters in R^2 and R^n.

VII. MODEL EVALUATION AND RESULTS

A novel algorithm always needs to be evaluated first before being applied to the target problem. First, the artificial dataset used to evaluate the proposed algorithm is randomly selected to have three subsets (*i.e.*, iris setosa, iris versicolor, and iris virginica), two of which are overlapping [50]. The iris data are in a four-dimensional space and there are a total of 150 patterns in the set. There are 50 data points for each of the three species. First, the Sammon's projection algorithm is used to project the iris data set into a 2-dimensional plot, as shown in Figure 11. By disregarding those isolated points or small clusters, as shown in Figure 11, the number of clusters in the data set can be roughly estimated by counting the number of major clusters.

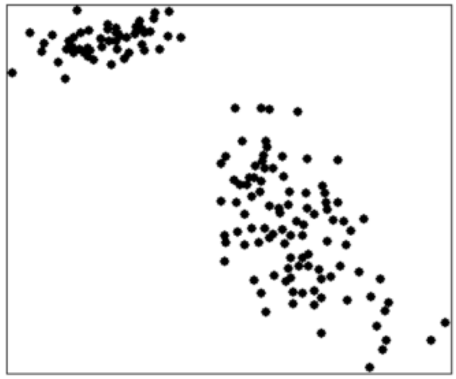

FIGURE 11. The projection result for the iris data set as obtained by Sammon's algorithm.

Obviously, there are only two major clusters. By further examining the scatter plot, we find that the larger cluster consists of an iris versicolor subset and iris virginica subset. The smaller cluster consists of the iris setosa subset. This observation is consistent with *a priori* knowledge about the iris data set. By viewing Figure 12, one may find that the PSOP algorithm presents two major clusters for the four settings of the value of the k.

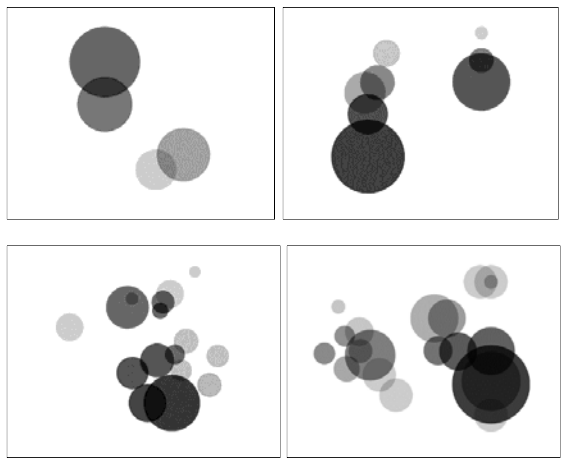

FIGURE 12. The projection results of the iris data set by the PSOP algorithm with: (a) k = 4. (b) k = 8. (c) k = 16. (d) k = 20.

This observation is consistent with Sammon's projection. As for the PSOP-stress algorithm, Figure 13 also presents two major clusters.

The results of a comparison of the computational efficiency are tabulated in Table 1. Obviously, Sammon's algorithm required the highest computational load.

Next, we apply the proposed algorithm for the recognition of CT images. The image data collected from the CT scan results are analyzed by applying both Sammon's and the PSOP algorithm. Figure 14 shows the property labeling of the concrete cylinder section and the sample indicators, respectively.

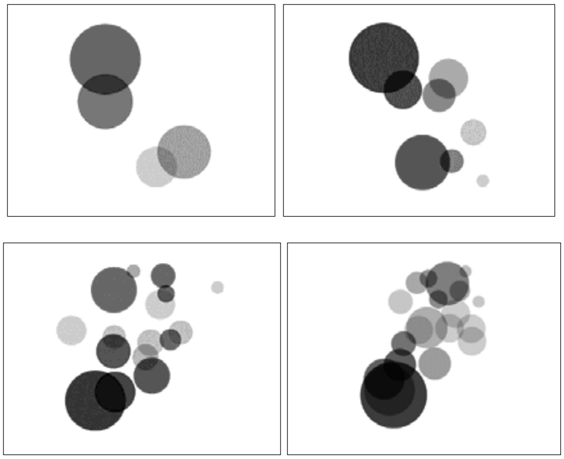

FIGURE 13. **The projection results of the iris data set by the PSOP-stress algorithm with: (a) k = 4. (b) k = 8. (c) k = 16. (d) k = 20.**

TABLE 1. **The computational efficiency comparisons for the iris data set.**

	Sammon	PSOP			
Time	9.37	K=4	K=8	K=16	K=20
(sec)		7.3×10^{-2} $\pm 1.3 \times 10^{-3}$	2.7×10^{-1} $\pm 5.7 \times 10^{-2}$	8.8×10^{-1} $\pm 4.7 \times 10^{-2}$	1.5 ± 5.1 $\times 10^{-1}$
		PSOP-stress			
		K=4	K=8	K=16	K=20
		8.5×10^{-2} $\pm 1.8 \times 10^{-3}$	2.9×10^{-1} $\pm 4.1 \times 10^{-2}$	9.0×10^{-1} $\pm 7.5 \times 10^{-2}$	1.8 ± 6.2 $\times 10^{-1}$

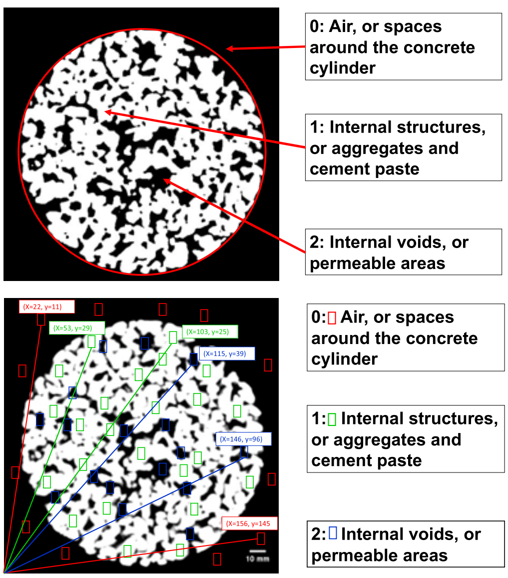

FIGURE 14. **Property labeling and sample indicators with coordinates.**

We used Sammon's algorithm for the real-life image data, and the result indicates only two major clusters with a few outliers. This does optimize our results from the CT scan, but it is not enough for us to derive a concrete explanation. After then proceeding with the PSOP algorithm, the observations are still consistent with the observations discussed in the previous section. By studying Figure 15, it is evident that the PSOP algorithm presents two major clusters for the four settings with a value of k.

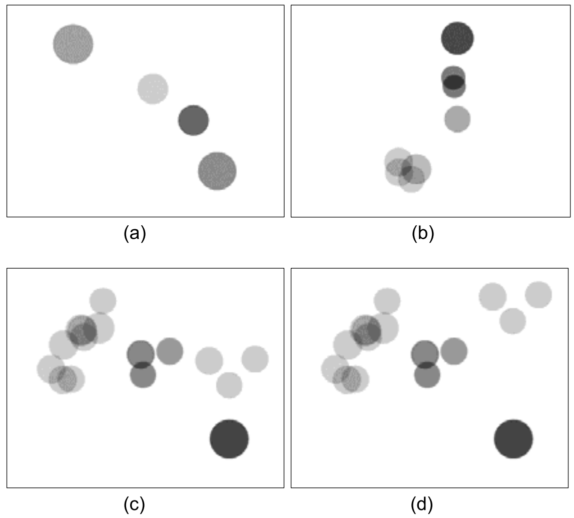

FIGURE 15. **The projection results for the real-life image data set by the PSOP algorithm with: (a) k = 4. (b) k = 8. (c) k = 16. (d) k = 20.**

This observation is consistent with Sammon's projection. Like the PSOP algorithm, the PSOP-stress algorithm, Figure 16 also presents two major clusters.

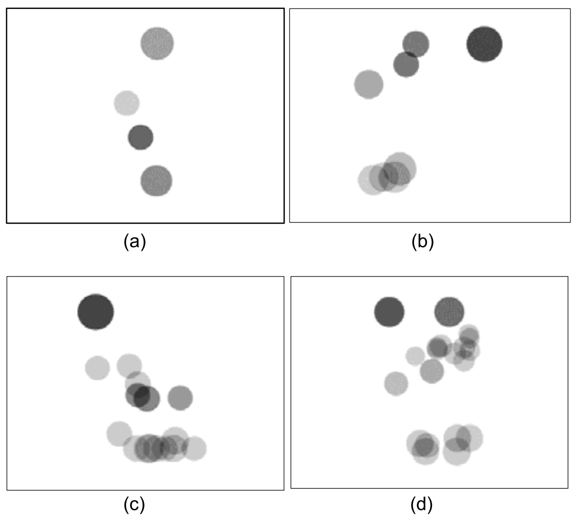

FIGURE 16. **The projection results for the real-life image data set by the PSOP-stress algorithm with: (a) k = 4. (b) k = 8. (c) k = 16. (d) k = 20.**

The results of a comparison of the computational efficiency are tabulated in Table 2. It is obvious that Sammon's algorithm required the highest computational load yet again. It is clear that by using the PSO-based projection algorithm, we have improved upon Sammon's algorithm, which is a non-linear projection algorithm.

TABLE 2. **The computational efficiency comparisons for the image data set.**

	Sammon	PSOP			
Time (sec)	7737.498	K=4	K=8	K=16	K=20
		4.57±7.2 x10^{-1}	7.37±3.7 x10^{-1}	1.54 x10^{1}±7.8 x10^{-1}	1.83 x10^{1}±9.5 x10^{-1}
		PSOP-stress			
		K=4	K=8	K=16	K=20
		5.81± 7.9x10^{-1}	7.79± 2.5x10^{-1}	1.96 x10^{1}± 4.3 x10^{-1}	1.839 x10^{1}± 8.6x10^{-1}

Figure 17 shows both the rough circle and the optimized circle obtained by the PSO algorithm. We adopted the PSOP-algorithm to fine-tune the circles initialized in the previous step.

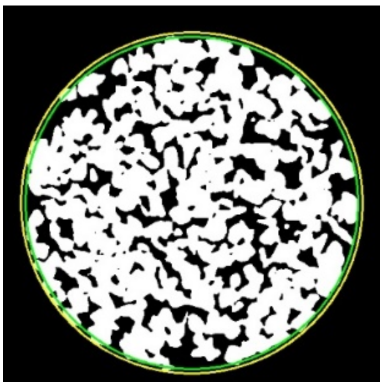

FIGURE 17. **The fine-tuned circle highlighted in yellow.**

Recently, the proposed PSO algorithm has received a lot of attention for different fields [39]–[41]. The PSO algorithm is similar to some evolutionary algorithms (e.g., the genetic algorithm) in the way that they all are initialized with a population of individuals (e.g., particles in the PSO and chromosomes in the genetic algorithm). However, the simulation of social learning behaviors (e.g., imitation, cooperation, and competition) rather than the evolutionary mechanisms (e.g., reproduction, crossover, and mutation) in evolutionary algorithms has motivated the development of the PSO. We adopted the PSO algorithm to fine-tune the center, (x, y), and the diameter, d, of the circle found in step 3 of section 3.2. To fine-tune the parameters of the circle, each particle is regarded as a three-dimensional vector consisting of information about the center, (x, y), and the diameter, d, of the circle. The objective of the optimization is to find the circle with the minimum diameter subject to the constraint of including all white points (i.e., the concrete pillar). In our simulations, the number of particles was set to be 100, the maximum number of iterations was 100, the maximum velocity was set to 10 and the inertial weight decreased linearly from 0.9 to 0.4. The resultant circle is displayed in Figure18. It is obvious that the fine-tuned circle is more appropriate than the initial circle found in Step 3. The white area (VFA) covers 75.01% of the total within the cylinder boundary, indicating a porosity rate of 24.99%. By referring to Equations (1) and (2), the porosity rate is 25%, and the accuracy rate > 99%.

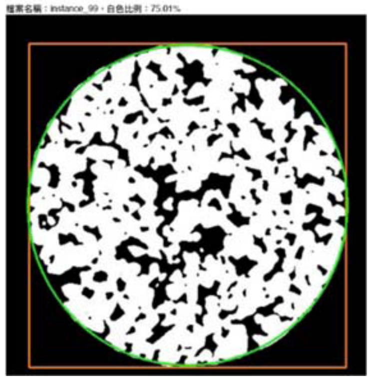

FIGURE 18. **Analyzed result.**

VIII. CONCLUSION

An automatic porosity detection model using a novel PSOP algorithm was built to detect and determine the porosity rate based on CT images of concrete cylinders. In order to make the images easier to analyze, it the removal of unnecessary information from the images is required. Therefore, we used 3-connectivity steps to remove text from the images after the CT scan. The first step was to produce a rectangle bounding the concrete cylinder and find the average of the widths and lengths is the rough diameter of the circle surrounding the concrete cylinder. Then, to get a more precise diameter, we adopted the PSOP algorithm to fine-tune the rough circle into an optimized circle in order to increase the accuracy of the circle surrounding the concrete cylinder. After the circle was formed, by using pattern recognition image processing, we derived the structure ratio of the concrete cylinder with an accuracy > 99%. Finally, after combining the series of images from the CT scan and PSOP, we found the porosity of the concrete cylinders.

By consulting the model created from this study, the process of determining the porosity or other properties of pervious concrete is considerably quicker and efficient. By using the proposed model, the images provided by a CT scan and further optimized by the PSOP can reveal the inner structure, obtain the permeability of a core drill specimen, and at the same time, assist pavement engineers in making better decisions through visualized images for maintaining road quality. We believe this study can contribute to improving the pavement management system worldwide. The pilot study is still an ongoing project and more outcomes will be unveiled in the near future. We also recommend future research into the correlation between the voids and permeability of concrete.

REFERENCES

[1] P. A. Claisse, J. G. Cabrera, and D. N. Hunt, "Measurement of porosity as a predictor of the durability performance of concrete with and without condensed silica fume," *Adv. Cement Res.*, vol. 13, no. 4, pp. 165–174, Oct. 2001.
[2] M. S. Sumanasooriyaa and N. Neithalath, "Pore structure features of pervious concretes proportioned for desired porosities and their performance prediction," *Cement Concrete Compos.*, vol. 33, no. 8, pp. 778–787, Sep. 2011.
[3] V. M. Sánchez-Fajardoa, M. E. Torresa, and A. J. Morenob, "Study of the pore structure of the lightweight concrete block with lapilli as an aggregate to predict the liquid permeability by dielectric spectroscopy," *Construct. Building Mater.*, vol. 53, pp. 225–234, Feb. 2014.
[4] R. He, H. Ma, R. B. Hafiz, C. Fu, X. Jin, and J. He, "Determining porosity and pore network connectivity of cement-based materials by a modified non-contact electrical resistivity measurement: Experiment and theory," *Mater. Design*, vol. 156, pp. 82–92, Oct. 2018.
[5] K. Zhanga, Z. Zhang, Y. Luo, and S. Huanga, "Accurate detection and evaluation method for aggregate distribution uniformity of asphalt pavement," *Construct. Building Mater.*, vol. 152, pp. 715–730, Oct. 2017.
[6] L. Gao, H. Li, J. Xie, Z. Yu, and S. Charmot, "Evaluation of pavement performance for reclaimed asphalt materials in different layers," *Construct. Building Mater.*, vol. 159, pp. 561–566, Jan. 2018.
[7] V. Bindiganavile, M. Mamun, B. Dashtestani, and N. Banthia, "Correlating the permeability of mortar under compression with connected porosity and tortuosity," *Mag. Concrete Res.*, vol. 70, no. 17, pp. 875–884, Sep. 2018.
[8] A. S. Braswell, R. J. Winston, J. Ryan, and W. F. Hunt, "Hydrologic and water quality performance of permeable pavement with internal water storage over a clay soil in Durham, North Carolina," *J. Environ. Manage.*, vol. 224, pp. 277–287, Oct. 2018 .
[9] J. Monrose and K. Tota-Maharaj, "Technological review of permeable pavement systems for applications in small island developing states," *Clean-Soil Air Water*, vol. 46, no. 9, p. 1700168, Sep. 2018.
[10] Y. Liu, T. Li, and H. Peng, "A new structure of permeable pavement for mitigating urban heat Island," *Sci. Total Environ.*, vol. 634, pp. 1119–1125, Sep. 2018.
[11] G. L. Balázs, E. Lublóy, and T. Földes, "Evaluation of concrete elements with X-ray computed tomography," *J. Mater. Civil Eng.*, vol. 30, no. 9, p. 06018010, Sep. 2018.
[12] X.-J. Li and X.-N. Zhang, "Application of X-ray computerized tomography in analysis of inner structure of asphalt mix," *J. Highway Transp. Res. Develop.*, vol. 22, pp. 14–16, Jan. 2005.
[13] X. Qin and Q. Xu, "Statistical analysis of initial defects between concrete layers of dam using X-ray computed tomography," *Construct. Building Mater.*, vol. 125, pp. 1101–1113, Oct. 2016.
[14] J. Deng, "Parallel computing techniques for computed tomography," Ph.D. dissertation, Dept. Appl. Math. Comput. Sci., Univ. Iowa, Iowa City, IA, USA, 2011.
[15] D. Wildenschild and A. P. Sheppard, "X-ray imaging and analysis techniques for quantifying pore-scale structure and processes in subsurface porous medium systems," *Adv. Water Resour.*, vol. 51, pp. 217–246, Jan. 2013.
[16] J.-W. Seo, D.-W. Park, and T. H. M. Le, "Development of an asphalt concrete mixture for Asphalt Core Rockfill Dam," *Construct. Building Mater.*, vol. 140, pp. 301–309, Jun. 2017.
[17] R. Mirzanamadi, P. Johansson, and S. A. Grammatikos, "Thermal properties of asphalt concrete: A numerical and experimental study," *Construct. Building Mater.*, vol. 158, pp. 774–785, Jan. 2018.
[18] S. M. Abraham and G. D. R. N. Ransinchung, "Strength and permeation characteristics of cement mortar with reclaimed Asphalt pavement aggregates," *Construct. Building Mater.*, vol. 167, pp. 700–706, Apr. 2018.
[19] A. Kia, H. S. Wong, and C. R. Cheeseman, "Defining clogging potential for permeable concrete," *J. Environ. Manage.*, vol. 220, pp. 44–53, Aug. 2018.
[20] J. Liu and M. Borst, "Performances of metal concentrations from three permeable pavement infiltrates," *Water Res.*, vol. 136, pp. 41–53, Jun. 2018.
[21] A. J. Ramsey, M. L. Hart, and J. T. Kevern, "Nutrient removal rates of permeable reactive concrete," *J. Sustain. Water Built Environ.*, vol. 4, no. 2, p. 4018004, May 2018.
[22] M. Shafique, R. Kim, and K.-H. Kwon, "Rainfall runoff mitigation by retrofitted permeable pavement in an urban area," *Sustainability*, vol. 10, no. 4, p. 1231, Apr. 2018.
[23] M. Razzaghmanesh and S. Beecham, "A review of permeable pavement clogging investigations and recommended maintenance regimes," *Water*, vol. 10, no. 3, p. 337, Mar. 2018.
[24] A. K. Jain and R. C. Dubes, *Algorithms for Clustering Data*. Englewood Cliffs, NJ, USA: Prentice-Hall, 1988.
[25] F. Höppner, F. Klawonn, R. Kruse, and T. Runkler, *Fuzzy Cluster Analysis: Methods for Classification, Data Analysis and Image Recognition*. Hoboken, NJ, USA: Wiley, 1999.
[26] J. C. Dunn, "Well-separated clusters and optimal fuzzy partitions," *J. Cybern.*, vol. 4, no. 1, pp. 95–104, Apr. 2008.
[27] J. C. Bezdek, "Numerical taxonomy with fuzzy sets," *J. Math. Biol.*, vol. 1, no. 1, pp. 57–71, May 1974.
[28] X. L. Xie and G. Beni, "A validity measure for fuzzy clustering," *IEEE Trans. Pattern Anal. Mach. Intell.*, vol. 13, no. 8, pp. 841–847, Aug. 1991.
[29] D. L. Davies and D. W. Bouldin, "A cluster separation measure," *IEEE Trans. Pattern Anal. Mach. Intell.*, vol. PAMI-1, no. 2, pp. 224–227, Apr. 1979.
[30] I. Gath and A. B. Geva, "Unsupervised optimal fuzzy clustering," *IEEE Trans. Pattern Anal. Mach. Intell.*, vol. 11, no. 7, pp. 773–780, Jul. 1989.
[31] R. N. Dave "Validating fuzzy partitions obtained through c-shells clustering," *Pattern Recognit. Lett.*, vol. 17, no. 6, pp. 613–623, May 1996.
[32] J. W. Sammon, "A nonlinear mapping for data structure analysis," *IEEE Trans. Comput.*, vol. C-18, no. 5, pp. 401–409, May 1969.
[33] P. Baldi and K. Hornik, "Neural networks and principal component analysis: Learning from examples without local minima," *Neural Netw.*, vol. 2, no. 1, pp. 53–58, 1989.
[34] H. M. Abbas and M. M. Fahmy, "A neural model for adaptive Karhunen Loeve transformation (KLT)," in *Proc. IEEE Int. Joint Conf. Neural Netw.*, Baltimore, MD, USA, Jun. 1992, pp. 975–980.
[35] E. Oja, "Simplified neuron model as a principal component analyzer," *J. Math. Biol.*, vol. 15, no. 3, pp. 267–273, Nov. 1982.
[36] J. Rubner and P. Schulten, "Development of feature detectors by self-organization," *Biol. Cybern.*, vol. 62, no. 3, pp. 193–199, 1990.
[37] M. A. Kraaijveld, J. Mao, and A. K. Jain, "A nonlinear projection method based on Kohonen's topology preserving maps," *IEEE Trans. Neural Netw.*, vol. 6, no. 3, pp. 548–559, May 1995.
[38] J. Mao and A. K. Jain, "Artificial neural networks for feature extraction and multivariate data projection," *IEEE Trans. Neural Netw.*, vol. 6, no. 2, pp. 296–317, Mar. 1995.
[39] N. R. Pal and V. K. Eluri, "Two efficient connectionist schemes for structure preserving dimensionality reduction," *IEEE Trans. Neural Netw.*, vol. 9, no. 6, pp. 1142–1154, Nov. 1998.
[40] M.-C. Su and H.-T. Chang, "A new model of self-organizing neural networks and its application in data projection," *IEEE Trans. Neural Netw.*, vol. 12, no. 1, pp. 153–158, Jan. 2001.
[41] J. Kennedy and R. Eberhart, "A new optimizer using particle swarm theory," in *Proc. 6th Int. Symp. Micro Mach. Hum. Sci.*, Nagoya, Japan, Oct. 1995, pp. 39–43.
[42] R. Eberhart and J. Kennedy, "A new optimizer using particle swarm theory," in *Proc. 6th Int. Symp. Micro Mach. Human Sci.*, Nagoya, Japan, Oct. 1995, pp. 39–43.
[43] J. Kennedy, R. C. Eberhart, and Y. Shi, *Swarm Intelligence*. New York, NY, USA: Academic, 2001.
[44] J.-H. Chen, "A hybrid knowledge-sharing model for corporate foreign investment in China's construction market," *Expert Syst. Appl.*, vol. 39, no. 9, pp. 7585–7590, 2012.
[45] J.-H. Chen, M.-C. Su, and L.-R. Yang, "Comparison of SOM-based optimization and particle swarm optimization for minimizing the construction time of a secant pile wall," *Autom. Construct.*, vol. 18, no. 6, pp. 844–848, 2009.
[46] J.-H. Chen, M.-C. Su, S.-I. Lin, and D.-Y. Huang, "SOM-optimized neurofuzzy classifiers for measuring expatriation willingness," *IEEE Intell. Syst.*, vol. 32, no. 5, pp. 28–34, Sep./Oct. 2017.
[47] J.-H. Chen, M.-C. Su, and B. A. Badjie, "Exploring and weighting features for financially distressed construction companies using swarm inspired projection algorithm," *Adv. Eng. Informat.*, vol. 30, no. 3, pp. 376–389, 2016.
[48] R. Liu and E. Sancaktar, "Identification of crack progression in filled rubber by micro X-ray CT-scan," *Int. J. Fatigue*, vol. 111, pp. 144–150, Jun. 2018.

[49] Y.-M. Su, M.-G. Lee, and G.-Y. Chen, "The exploration study of fire damage to concrete specimen using X-Ray computed tomography," *Proc. SPIE*, vol. 9437, p. 94370A, 2015.

[50] C. L. Blake and C. J. Merz. (1998). UCI repository of machine learning databases. University of California, Oakland, CA, USA. [Online]. Available: http://www.ics.uci.edu/~mlearn

YI-ZENG HSIEH received the B.S., M.S., and Ph.D. degrees in computer science and information engineering from National Central University, Taoyuan, Taiwan, in 2004, 2006, and 2012, respectively. He is currently an Assistant Professor of electrical engineering with National Taiwan Ocean University. His current research interests include neural networks, pattern recognition, image processing, and machine learning.

MU-CHUN SU received the B.S. degree in electronics engineering from National Chiao Tung University, Taiwan, in 1986, and the M.S. and Ph.D. degrees in electrical engineering from the University of Maryland, College Park, in 1990 and 1993, respectively. He is currently a Professor of computer science and information engineering with National Central University, Taiwan. He has authored more than 100 journal and refereed conference papers. His current research interests include computational intelligence, neural networks, fuzzy systems, swarm intelligence, affective computing, human–computer interaction, robotics, pattern recognition, biomedical signal processing, image processing, and rehabilitation technology. He is a Senior Member of the IEEE Computational Intelligence Society and the IEEE Systems, Man, and Cybernetics Society. He is also a fellow of IET. He was a recipient of the IEEE Franklin V. Taylor Award in 1991. He serves as an associate editor for many journals.

JIEH-HAUR CHEN received the B.S. degree in civil engineering from National Central University (NCU), Taiwan, in 1995, the M.S. degree in project management from Northwestern University, Evanston, IL, USA, in 1999, and the Ph.D. degree in civil engineering from the University of Wisconsin–Madison, Madison, WI, USA, in 2003.

Since 2004, he has been with the Civil Engineering Department, NCU. He has authored more than 150 articles. His research interests include computational intelligence, managerial finance in engineering, smart city applications, and property management. He is a Senior Member of the National Science Council Committee Board in the civil engineering area, Taiwan. He is also an editor of major engineering-related journals.

Dr. Chen has received the permanent Distinguished Professor title from NCU in 2013. His awards and honors include the Extraordinary Military Service Award in 1997, the College Outstanding Service Award in 2009, the NCU Outstanding Researcher Award of the Year in 2011 and 2012, the Special Contribution in Technical Transferring Award in 2015 and 2016, and the NCU Excellence in Service Award in 2017.

BEVAN ANNUERINE BADJIE (M'18) received the Technician Diploma degree in construction from the Gambia Technical Training Institute (G.T.T.I.), Banjul, Gambia, in 2005, the B.S. degree in civil engineering from the National Taipei University of Technology, Taipei, Taiwan, in 2012, and the M.S. degree in construction engineering and management from National Central University, Taoyuan, Taiwan, in 2014, where he is currently pursuing the Ph.D. degree in construction engineering and management.

He was an Assistant Lecturer and a Site Engineer for major projects at G.T.T.I. from 2005 to 2008. Since 2014, he has been taking part in major research projects as a supervisor/professor. He has co-authored a few articles. His research interest includes computational intelligence, managerial finance in engineering, property management, and sustainable design. He has reviewed and edited major engineering-related journals.

Mr. Badjie's awards and honors include the Excellence Award for Outstanding Academic Performance by the National Taipei University of Technology in 2011 and the Academic Research Ethics Award by the Center for Taiwan Academic Research Ethics Education in 2018. He also received numerous awards for participation in academic research conferences.

YU-MIN SU received the Ph.D. degree from the Department of Civil Engineering, University of Florida, Gainesville, FL, USA, in 2012. He has been an Assistant Professor with the Department of Civil Engineering, National Kaohsiung University of Science and Technology, Kaohsiung, Taiwan, since 2014. His research interests cover highway and pavement engineering, asset management, and smart technologies. He received the Fellowship of International Road Federation (IRF), Taiwan, in 2009. He has been serving as a Sector Coordinator for IRF, the Board of Director of the China Road Federation (CRF), a Member of Technical Committee for the Road Engineering Association in Asia and Australia, and a Member Of Program Committee for the SPIE Smart Structures/NDE.